4 Simulation of radiation environments

Editors: I. Dawson[a]*, S. Mallows*[b]*.*
Contibuting authors: A. Alici[c]*, I. Azhgirey*[d]*, I. Dawson*[a]*, M. Huhtinen*[e]*, V. Ivantchenko*[f]*, D. Kar*[g]*, M. Karacson*[e]*, S. Mallows*[b]*, T. Manousos*[e]*, I. Mandić*[h]*, A. Di Mauro*[e]*, S. Menke*[i]*, P.S. Miyagawa*[a]*, A. Oblakowska-Mucha*[j]*, S. Pospisil*[k]*, T. Szumlak*[j]*, V. Vlachoudis*[e]*.*
[a]Queen Mary University of London, United Kingdom
[b]Karlsruhe Institute of Technology, Germany
[c]University of Bologna, Italy
[d]IHEP, Protvino, Russia
[e]CERN, Geneva, Switzerland
[f]Tomsk State University, Russia
[g]University of the Witwatersrand, Johannesburg, South Africa
[h]Jozef Stefan Institute, Ljubljana, Slovenia
[i]Max Planck Institute for Physics, Munich, Germany
[j]AGH University of Science and Technology, Kraków, Poland
[k]Czech Technical University in Prague, Czech Republic

Simulating radiation environments is crucial in the design phase of new hadron collider experiments or upgrades, especially when extrapolating to new centre of mass collision energies where previous experience cannot be relied on. The generation of radiation fields in the LHC experiments is dominated by proton–proton collisions, with contributions from beam-gas interactions and other machine losses [1]. It is therefore essential to first reproduce the proton–proton collisions, using Monte Carlo event generators such as PYTHIA8 [2] and DPMJET-III [3]. This part of the simulation chain is discussed in Section 4.1.

The particles originating from the proton–proton collisions interact with the detector and machine material, causing electromagnetic and hadronic showers which give rise to the complex radiation fields seen in the LHC experiments. This second part of the simulation is dealt with using advanced Monte Carlo particle transport codes such as FLUKA [4,5], MARS [6], or GEANT4 [7]. An overview of these codes is given in Section 4.2.

Key radiation quantities of interest are extracted from the simulations, such as 1 MeV neutron equivalent fluence and total ionizing dose, and these are discussed in Section 4.3. It is these quantities that are needed by the detector systems for evaluating radiation damage and predicting sensor and electronic performance over the lifetime of the experiment. In Section 4.4, the simulated predictions of radiation backgrounds for each of the experiments is presented. Finally, in Section 4.5, we offer general conclusions and recommendations for the future.

4.1 Event generation

The physics processes in inelastic proton–proton collisions are dominated by soft (low-p_T) QCD interactions, but hard (high-p_T) parton–parton scatters can play an important role too in radiation background studies. Experimental physicists often refer to these events as ‘minimum bias’, reflecting the minimally biassed trigger system required to study these events. Although the hard scattering processes are well described by perturbative QCD, this breaks down for low-p_T interactions and a wide variety of models with distinct theoretical concepts have been developed to describe this regime.

This chapter should be cited as: Simulation of radiation environments, Eds. I. Dawson, S. Mallows, DOI: 10.23731/CYRM-2021-001.35, in: Radiation effects in the LHC experiments and impact on detector performance and operation, Ed. Ian Dawson, CERN Yellow Reports: Monographs, CERN-2021-001, DOI: 10.23731/CYRM-2021-001, p. 35.

A good minimum-bias event generator describes accurately both the soft and hard physics processes, including diffractive disassociation of one or both protons. The cross-sections for these processes should be provided too so that event rates can be calculated. Another desirable feature is a smooth transition between the soft and hard processes up to the highest centre-of-mass collision energies. PHOJET [8] (part of the DPMJET-III package) was used extensively during the design phase of the ATLAS experiment, and implements the dual parton model [9] to describe particle production in low-p_T processes. PYTHIA6 was also used in the original design studies on ATLAS and LHCb to provide an estimate of systematic uncertainties in the event generator predictions. PYTHIA6 implements leading-order QCD matrix elements with a very low transverse momentum cutoff to model the low-p_T (non-diffractive) physics, and incorporates different approaches for dealing with the resulting divergences. Other well-known Monte Carlo event generators at the time, such as ISAJET and HERWIG, had not been fully developed for minimum-bias event generation.

Collision data taking began in earnest at the LHC experiments in 2010, and comparisons with the Monte Carlo predictions have been made. Measurements of event distributions such as $\mathrm{dN_{ch}}/\mathrm{d}\eta$ and $\mathrm{dN_{ch}}/\mathrm{d}p_T$ have been made for centre-of-mass energies 900 GeV, 7 TeV, and 13 TeV. Examples of measurements compared with event generator predictions from ATLAS [10] and LHCb [11] are shown in Figs. 20 and 21, respectively. Examples of measurements from CMS compared with event generator predictions are found in Ref. [12].

Corresponding measurements of the proton–proton cross-sections have also been made, allowing the rise of the inelastic cross-sections to be studied [13]. Shown in Table 5 is a comparison of the predicted and measured proton–proton cross-sections between the experiments. The ATLAS and LHCb experiments use mainly PYTHIA8 for minimum-bias event generation. This is because the code is fully supported by the LHC experiments and the code authors, with continuous development and improvement of the physics models. DPMJET-III is integrated into the FLUKA transport code and is used by CMS.

Table 5: Inelastic proton–proton cross-sections (mb) measured by the LHC experiments. These are compared with the PYTHIA8 cross-sections used by ATLAS for MC event generation. The DPMJET-III prediction for $\sqrt{s}$ =13 TeV is 84 mb.

	LHC measurements			**PYTHIA8**
	ATLAS	**CMS**	**LHCb**	**(ATLAS tune)**
$\sqrt{s}$ =13 TeV	78.1 ± 2.9	71.3 ± 3.5	75.4 ± 5.4	78.4
$\sqrt{s}$ =7 TeV	69.1 ± 2.4	64.5 ± 3.2	66.9 ± 5.3	71.4

4.2 Particle transport codes

Monte Carlo particle transport codes are essential in simulating and studying the radiation fields. The main workhorse codes for ATLAS during the design phase were FLUKA and GCALOR, but today (2020) most radiation background studies are performed with FLUKA and GEANT4. CMS continues to use both FLUKA and MARS for radiation background studies. Both LHCb and ALICE have relied principally on FLUKA for radiation particle transport since early design studies.

4.2.1 FLUKA

The FLUKA code [4,5] is well established for studies of hadronic and electromagnetic cascades induced by high-energy particles and it is the baseline code for radiation background simulations at CERN and the LHC experiments. Electrons, photons, and muons can be interacted and transported up to 1000 TeV, and hadrons up to 20 TeV. Lower transport limits are typically at the keV level, except for low-energy

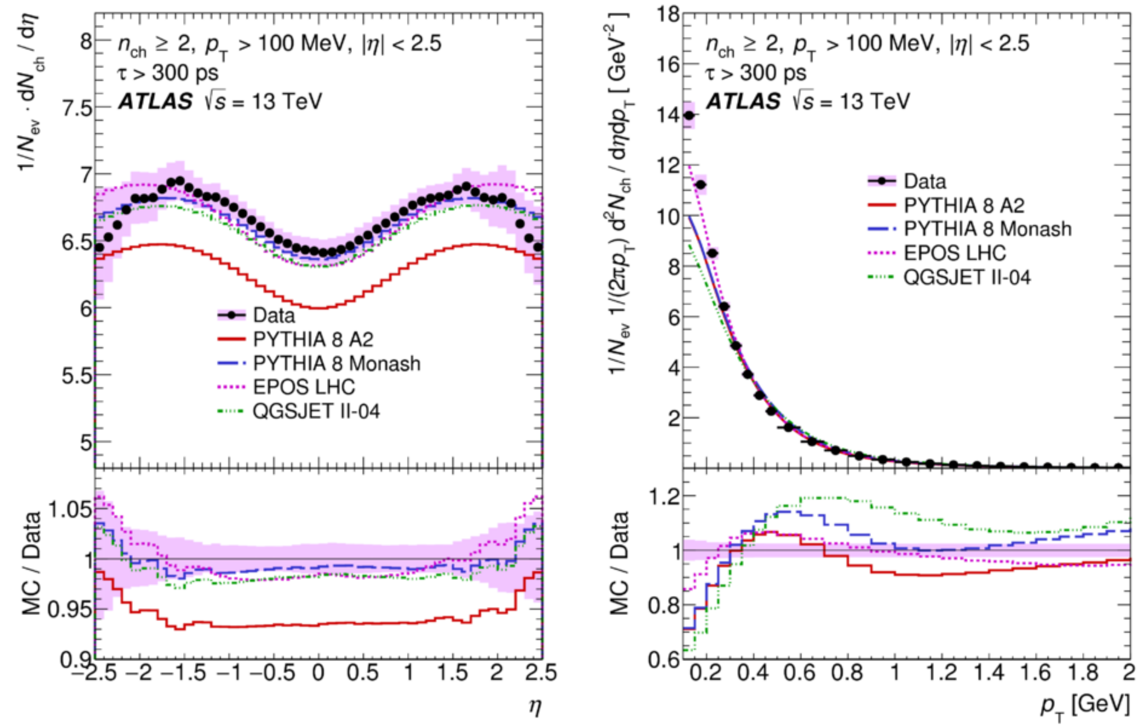

Fig. 20: Primary charged particle multiplicities as a function of (left) pseudorapidity η and (right) transverse momentum p_{T} for events with at least two primary charged particles with $p_{\mathrm{T}} > 100\,\mathrm{MeV}$ and $|\eta| < 2.5$, each with a lifetime $>$ 300 ps. The black dots represent the data and the coloured curves the different MC model predictions. The plots are taken from Ref. [10].

neutrons which can be transported to thermal energies. Anti-particles, heavy ions, and residual nuclei production are also treated by FLUKA.

Microscopic physics modelling is adopted in FLUKA when possible and conservation laws are enforced at each interaction step. Results are benchmarked against experimental data at the single interaction level. An advantage of this methodology is that the simulated predictions are based on a minimal set of free parameters which are fixed for all projectile energies and target materials. This makes simulations more reliable when extrapolating to complex cases where no experimental data exists, and correlations within interactions and shower components are preserved.

A complete description of FLUKA's physics models and capabilities can be found in Ref. [14] and references therein. As an example, inelastic hadron interactions are described by different physics models depending on the energy. For inelastic hadron–hadron interactions above 5 GeV the dual parton model (DPM) [15] is used, and below 5 GeV the resonance production and decay model [16]. For hadron–nucleus inelastic interactions greater than 5 GeV, Glauber–Gribov multiple scattering followed by generalized intranuclear cascade (GINC) is employed. Below 5 GeV, the pre-equilibrium-cascade model PEANUT is used [17, 18]. All the above hadron interaction models include evaporation and gamma deexcitation of the residual nucleus [19, 20]. Light residual nuclei are not evaporated but fragmented into a maximum of 6 bodies according to a Fermi break-up model.

For the geometry and material description, FLUKA uses a 'combinatorial geometry' which combines bodies (defined by surfaces) into regions using boolean operations (union, subtraction, etc.). The transport and interaction of particles in FLUKA are also designed to accurately track charged particles in the presence of magnetic or electric fields. Although intrinsically an analogue code, FLUKA can be

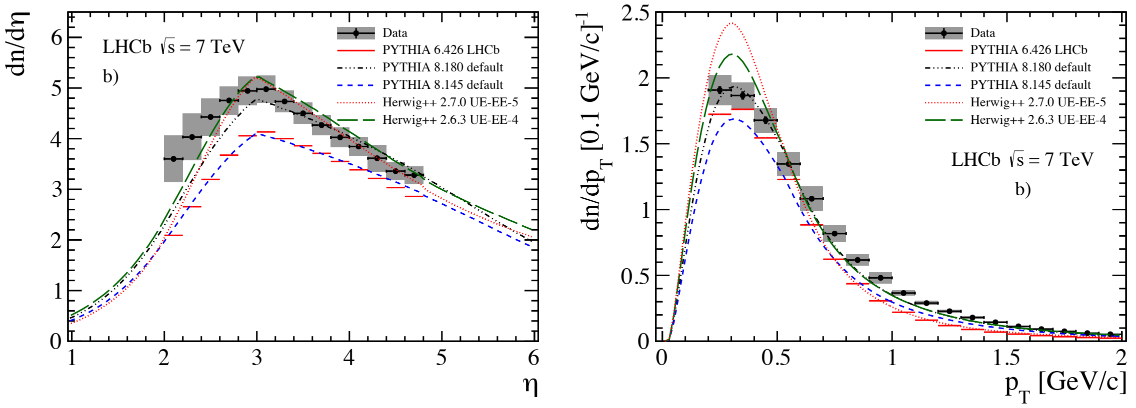

Fig. 21: Charged particle density as a function of η (left) and p_{T} (right). The LHCb data are shown as points. The grey bands are the combined systematic and statistical uncertainties. The measurements are compared to several Monte Carlo generator predictions. The plots are taken from Ref. [11].

run in biased mode (variance reduction) for a variety of deep penetration applications.

4.2.2 MARS

The Monte Carlo simulation package MARS [6] is occasionally used to calculate the radiation levels in the CMS cavern, and was used by ATLAS in the very early days of shielding design. MARS is similar to FLUKA, but the main difference is that it is an inclusive code, so that a fixed number of secondary particles is generated in one step, with weights according to the averaged multiplicities of such particles. MARS uses a 28-group library for low-energy (< 14.5 MeV) neutron reactions and transport, while photon production in low-energy neutron-induced reactions is described in a 15-group approximation.

4.2.3 GEANT4

GEANT4 [7] is a toolkit for simulating the passage of particles through matter and is used by all the LHC experiments for studying detector performance. It is the outcome of an international collaboration of physicists and software engineers, exploiting the advantages of modern object-oriented programming and, in contrast FLUKA and MARS, constructed to allow easy access to the physics models.

However, the use of GEANT4 for radiation background studies in the past has been limited. Radiation transport codes such as FLUKA and MARS were more established in accurately modelling both high- and low-energy nuclear physics processes. Today, the situation has changed and the increasingly mature GEANT4 is now considered a credible alternative for HEP radiation background studies.

Physics lists are used to configure the physics processes to be enabled in the simulation. The default physics simulation list (since version 9.6) is the so-called FTFP_BERT, but for radiation background studies either the FTFP_BERT_HP or SHIELDING lists are recommended as they enable high precision neutron transport. Users can also customize lists to their needs, for example adding a radioactive decay package.

An interesting development ($\sim$2018) by the ATLAS experiment was to run their full GEANT4 physics simulation framework, which uses a very detailed description of the ATLAS detector, with physics settings appropriate for radiation background studies. In the past this was not feasible due to CPU and memory issues, but today running on the GRID has made this possible.

4.2.4 GCALOR

The GCALOR package [21] was used extensively for ATLAS radiation background studies during the initial design phase. It was developed and maintained by the Oak Ridge National Laboratory, and was one of the recommended detector simulation codes to support the development of detector designs for the Superconducting Super Collider project in the 1990s.

By the time of LHC upgrade studies, the support for CALOR and GEANT3 maintenance and development was limited, and FLUKA, MARS and GEANT4 became the preferred choice for radiation background studies. We also make the point that radiation background expertize tends to be limited, so sometimes it is better to be agnostic when it comes to choosing simulation strategies.

4.3 Radiation damage estimators

The radiation environments at the LHC experiments are complex, covering a wide range of particle types and energies. In practice, only a few derived quantities are needed to predict detector damage and performance. The physics of radiation effects on sensors and electronics is described in Section 2. The three main radiation quantities of interest are:

- the 1 MeV neutron equivalent fluence ($\Phi_{\mathrm{eq}}^{\mathrm{Si}}$), allowing studies of bulk damage in silicon and the impact on electrical and optical properties, such as leakage currents, depletion voltages, and charge collection efficiency. The particle type and energy is obtained from the simulations and scaled by the hardness factors described in Section 2. The hardness factors have been experimentally determined only over limited energy ranges for neutrons, protons and pions, and the associated uncertainties are estimated to be $\sim 30\%$;
- total ionizing dose (TID), defined as the amount of ionizing energy deposited per unit mass of material. In the design and qualification of electronics the ionizing radiation can lead to charges trapped in the device oxide layers. The accumulated charge can induce shifts in device threshold voltages and increased parasitic currents. In addition, scintillating materials and optical fibres also suffer from damage that to good approximation is proportional to the ionizing dose. The damage manifests itself as a reduction of the light transmission, as induced phosphorescence, or changes of the scintillating properties;
- hadron fluence > 20 MeV (Φ_{20}^{had}). This characterization of the radiation field is used for predicting single event upsets (SEU) estimates at the LHC [22]. Single event effects (SEE) in electronic circuits are caused by large energy depositions close to sensitive regions of the chips. The released charge can be sufficient to flip the logic state of a transistor, and in extreme cases cause permanent or destructive damage. The amount of ionization needed to cause a SEE can be only deposited by heavy ions, which at the LHC can be created in the chip itself from high-energy hadron interaction with the target nuclei.

4.4 Experiment simulations and predictions

4.4.1 ATLAS

The radiation environment in the ATLAS inner detector is complex and comprises a full spectrum of particles (pions, protons, neutrons, photons, etc.), with energies ranging from TeV down to thermal for neutrons. Close to the interaction point the environment is dominated by particles coming directly from the proton–proton collisions, but at larger radii albedo neutrons from high-energy hadron and electromagnetic cascades in the calorimeters can play a major role. The use of advanced Monte Carlo event generators and particle transport codes is the principle method for accurately simulating and studying such complex radiation environments.

The deleterious effects of radiation in silicon sensor systems include: increased leakage currents; charge accumulation in silicon oxide layers; decreasing signal-to-noise; changing depletion voltages;

single event effects impacting electronics; and radiation-induced activation of components. Both sensors and electronics are impacted by radiation and the measurements and observations made in these two areas are discussed in detail in Sections 5 and 6, respectively.

Radiation background simulations on ATLAS have been performed mainly using the FLUKA particle transport code since the first design studies, with GCALOR playing a big role too. More recently GEANT4 simulations have been performed successfully for radiation background studies which uses the same simulation framework as for the physics performance studies and thus exploits the full detailed ATLAS geometry description. See Section 4.2 for a description of these codes.

PYTHIA8 is used to generate the inelastic proton–proton collisions (including single and double diffractive processes) which feed into the FLUKA and GEANT4 simulations. In particular, PYTHIA8 is tuned to LHC minimum-bias data [23] and events are generated according to the LHC centre of mass energies (7, 8, and then 13 TeV). The ATLAS PYTHIA8 tune predicts a fiducial inelastic cross-section of 69.9 mb at 13 TeV, which compares well with the measured value of 68.1 ± 1.4 mb. In the original FLUKA studies, the PHOJET event generator was used. The predictions for the fluences in the inner detector are typically $\sim 5\%$ higher with PYTHIA8 than for PHOJET. More details about the event generators are given in Section 4.1.

FLUKA simulation studies are typically performed on CPU farms, with the codes installed locally on Unix based workstations. The ever increasing CPU capacity has benefitted ATLAS simulations enormously over the past 20 years allowing faster turnaround times and increasing detector description complexity. The situation was similar for the original GCALOR and MARS simulation effort. Eventually, around 2014, FLUKA started using the SVN repository, and later GIT, to allow shared collaboration and file versioning between the different groups performing FLUKA simulations. GEANT4 simulation studies take advantage of the ATLAS GeoModel detector description [24] and jobs are run on the GRID. Simulation results are shared with the various experiment groups through Web tools and TWiki pages.

4.4.1.1 ATLAS detector geometry and material description

For the accurate simulation of radiation environments, a well-defined geometry model is needed which includes the detector systems, shielding elements, services, and beam-line material. Details of the inner detector system are described in Section 3.2.1. An overview of the full ATLAS experiment can be found in Ref. [25]. Shown in Fig. 22 is the inner detector region as described in the FLUKA geometry. A complete description of the surrounding calorimeters is also important to reproduce the neutron albedo. For the most part the FLUKA geometry is simplified, describing for example detector barrel layers as cylinders. This is sufficient (in most cases) as long as the material radiation and interaction lengths are reproduced accurately. In contrast, the GEANT4/GeoModel detector description is built for physics performance simulations and contains millions of geometry volumes. In the past such simulations were prohibitively CPU expensive for radiation background studies, but these days running on the LHC computing Grid has made this feasible.

Running simulations with more than one simulation package allows comparisons to be made and investigations into simulation uncertainties. This is especially useful in regions where the geometry description is complex. Radiation background studies comparing FLUKA and GEANT4 suggest that differences in the physics models are small for the quantities of interest ($\Phi_{\mathrm{eq}}^{\mathrm{Si}}$, TID, Φ_{20}^{had}) and that in most cases it is the geometric uncertainties that are most important.

4.4.1.2 FLUKA fluence and dose predictions

FLUKA simulations of $\Phi_{\mathrm{eq}}^{\mathrm{Si}}$ and TID in the ATLAS inner detector region are shown in Fig. 23. Such r-z colour plots are common in ATLAS, superimposed on a quarter slice of the FLUKA geometry and illustrating how fluence and dose profiles vary across different regions. The fluence and dose values are averaged over ϕ. The radius r is measured from the beam line, and z from the interaction point. Similar

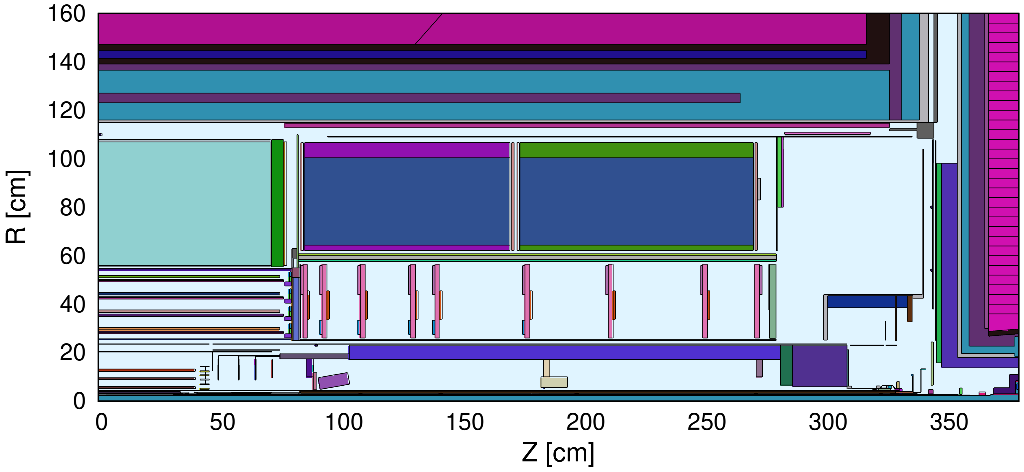

Fig. 22: ATLAS geometry described in FLUKA focusing on the inner detector regions, including part of the surrounding calorimeter (magenta).

plots are generated for Φ_{20}^{had} to allow SEE estimates. The locations of the IBL (insertable B-layer), pixels, SCT (semi-conductor tracker), and TRT (transition radiation tracker) are indicated.

Illustrated in Fig. 24 is the neutron component of $\Phi_{\mathrm{eq}}^{\mathrm{Si}}$ in the central region ($z = 0$) as a function of the radius r. In the IBL and pixel systems, $\Phi_{\mathrm{eq}}^{\mathrm{Si}}$ is dominated by charged pions from the IP, but once we reach the radii of the SCT it is the neutrons 'back splashing' from the calorimeters that matter. In the absence of scattering and a magnetic field, the particles emerging from the IP with a flat η-distribution[1] would result in a fluence independent of z and dropping as r^{-2}. Figure 24 shows that this radial dependence is well described up to $\mathrm{r} \sim 20$ cm, but in the SCT region the fluence shows a much slower decrease, which is due to the particle interactions and showering, as well as the effect of the 2 T inner detector solenoid field. Also shown is the FLUKA to GEANT4 ratio, where it can be seen that the GEANT4 predictions are some $\sim 20\%$ higher in the regions $r > 20$ cm, which is ascribed mainly to differences in the geometry and material description between the two codes.

While the colour plots and histograms illustrated above are useful for information dissemination within the collaboration, more important to the detector sub-systems are tables of values. As an example, given in Table 6 are the $\Phi_{\mathrm{eq}}^{\mathrm{Si}}$, TID and Φ_{20}^{had} values in the different module locations of the IBL.

4.4.1.3 Comparison of simulated predictions with measurements

The FLUKA and GEANT4 simulations on ATLAS provide crucial input into modelling radiation effects. Comparisons with measurements gives an indication of the simulation uncertainties which in turn allows future simulation accuracies to be evaluated. Section 5 describes in detail some of the measurements made on ATLAS and their comparison with model predictions. As an example, leakage current measurements from some four thousand SCT detector modules are combined to produce the plot given in Fig. 25. Differences between the predictions and measurements are typically less than 20%. However, larger differences are being observed in the outer Pixel barrel layers, some $\sim 50\%$ higher than the

---

[1] A reasonable approximation for pp collisions at the LHC and $|\eta| < 3$.

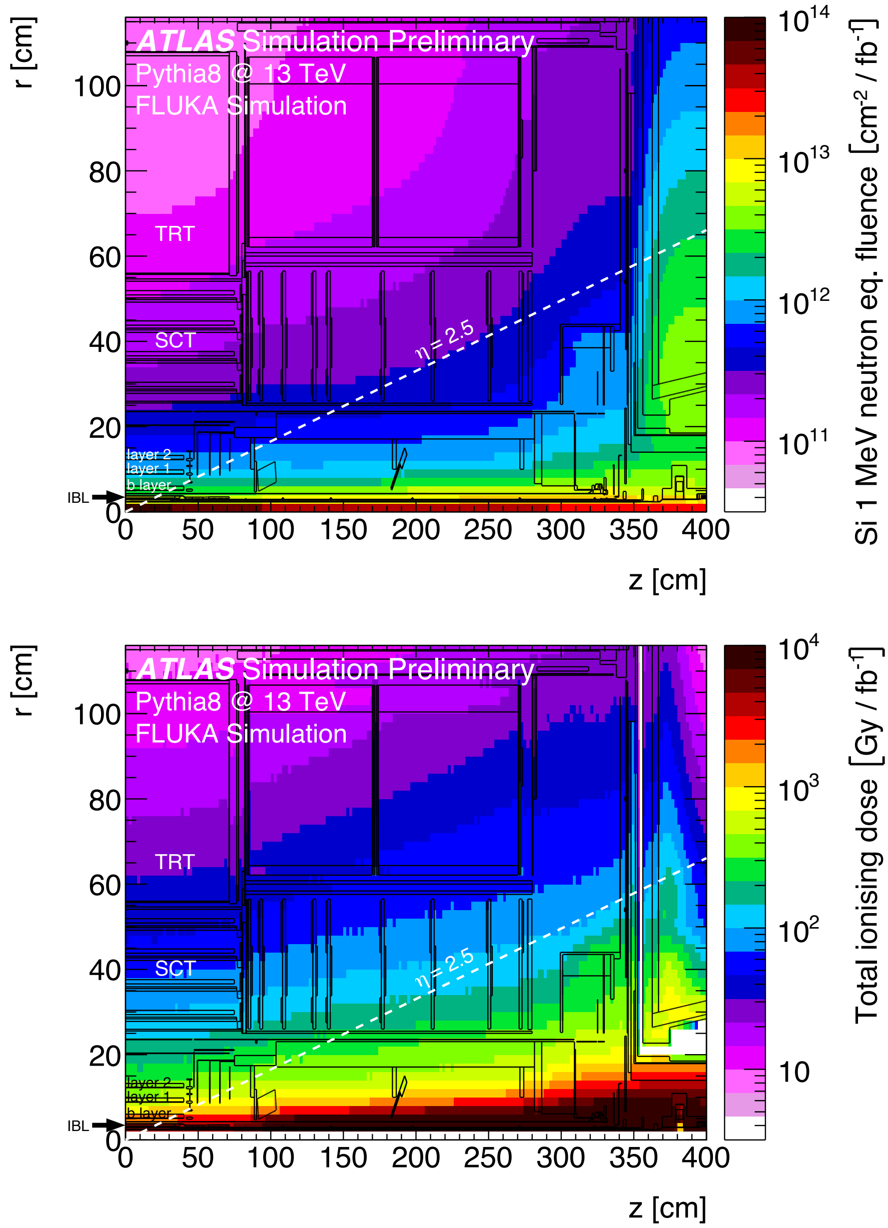

Fig. 23: The 1 MeV neutron equivalent fluence (top) and total ionizing dose (bottom) in the ATLAS inner detector. The minimum-bias pp events are simulated with ATLAS tuned Pythia8 at 13 TeV centreof-mass energy and a predicted inelastic cross-section of 78.4 mb. Particle tracking and interactions with material are simulated with the FLUKA 2011 code using the Run 2 geometry description of the ATLAS detector.

simulated predictions. In general this is more of a concern to experiments, when the simulations under predict the impact of radiation. The IBL and Pixel measurements and comparison with simulations are described in Section 5.

In addition to the Pixel and SCT sensor measurements, ATLAS also installed a radiation monitoring system. The so-called RadMon system [26, 27] consists of sensors at 14 locations inside the ID volume. In addition to $\Phi_{\mathrm{eq}}^{\mathrm{Si}}$, measurements of TID are made with the RadMons, which cannot be done with the silicon detector systems. These measurements and comparisons with simulated predictions are shown in Fig. 26. It can be seen that the FLUKA and GEANT4 predictions agree with each other,

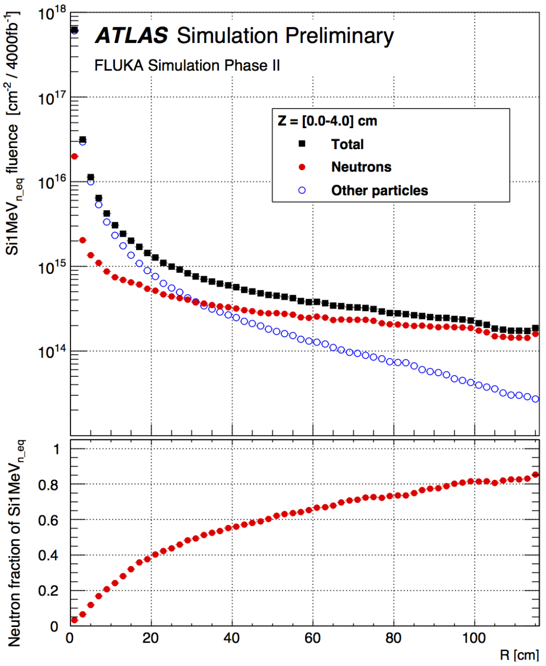

Fig. 24: Radial dependence of $\Phi_{\mathrm{eq}}^{\mathrm{Si}}$ at $z = 0$ as predicted by FLUKA. The total $\Phi_{\mathrm{eq}}^{\mathrm{Si}}$ is separated into the contribution from neutrons and all other particles.

Table 6: Fluence and dose values in the ATLAS IBL detector system predicted by FLUKA, based on 50 000 events. For Φ_{20}^{had}, the assumed instantaneous luminosity is $10^{34}\,\mathrm{cm}^{-2}\,\mathrm{s}^{-1}$.

IBL module	**Sensor** type	**z position** (cm)	$\mathbf{\Phi_{eq}^{Si}}$ ($\times 10^{11}\mathrm{cm}^{-2}/\mathrm{fb}^{-1}$)	**TID** (Gy /fb^{-1})	$\mathbf{\Phi_{20}^{had}}$ ($\times 10^{6}\,\mathrm{cm}^{-2}\,\mathrm{s}^{-1}$)
0	planar	2.08	62.5 ± 0.4	2897 ± 24	83.4 ± 0.4
1	planar	6.23	61.2 ± 0.3	2901 ± 23	85.0 ± 0.4
2	planar	10.38	59.7 ± 0.3	2917 ± 23	87.5 ± 0.4
3	planar	14.53	58.0 ± 0.3	2983 ± 26	89.0 ± 0.5
4	planar	18.68	56.6 ± 0.3	3015 ± 25	89.6 ± 0.5
5	planar	22.83	55.6 ± 0.4	3083 ± 27	89.4 ± 0.5
6	3D	25.94	55.2 ± 0.4	3126 ± 32	89.8 ± 0.6
7	3D	28.00	55.5 ± 0.4	3182 ± 34	90.6 ± 0.6
8	3D	30.07	55.0 ± 0.4	3191 ± 34	90.4 ± 0.6
9	3D	32.13	55.7 ± 0.4	3308 ± 36	91.0 ± 0.6

but overestimate compared with the measurements. Given the measurement uncertainties, the level of agreement is considered reasonable, being somewhat worse for the RadMon in the cryostat location.

In the original ATLAS design studies, ‘safety factors’ were introduced to reflect the uncertainties in simulating radiation backgrounds at the unprecedented centre-of-mass collision energy and luminosities. These were used for the testing and qualification of technologies for application in radiation environments. For example, in the testing and procurement of electronics, safety factors of 3.5 (5.0) were applied to the simulated radiation levels for TID ($\Phi_{\mathrm{eq}}^{\mathrm{Si}}$, Φ_{20}^{had}). A taskforce review in 2013 concluded it was reasonable to reduce these safety factors to 1.5 for all three radiation quantities.

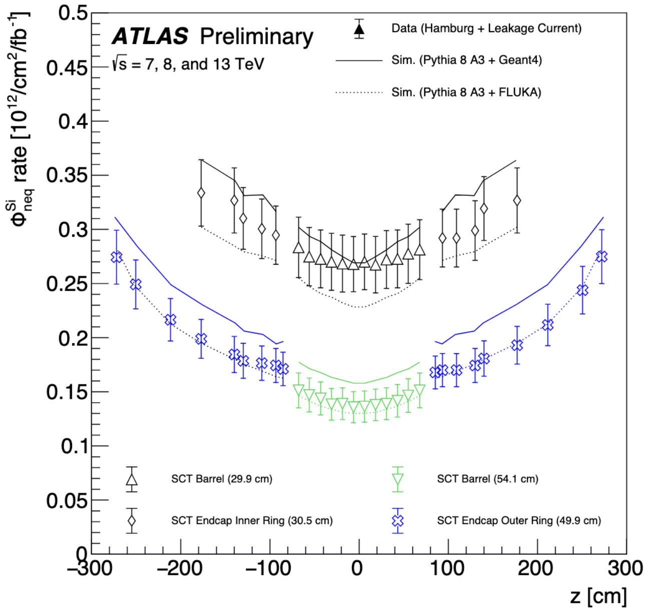

Fig. 25: Comparison of measured and simulated leakage current in the innermost and outermost SCT barrel and endcap layers. The simulations are based on FLUKA or GEANT with the Hamburg annealing model.

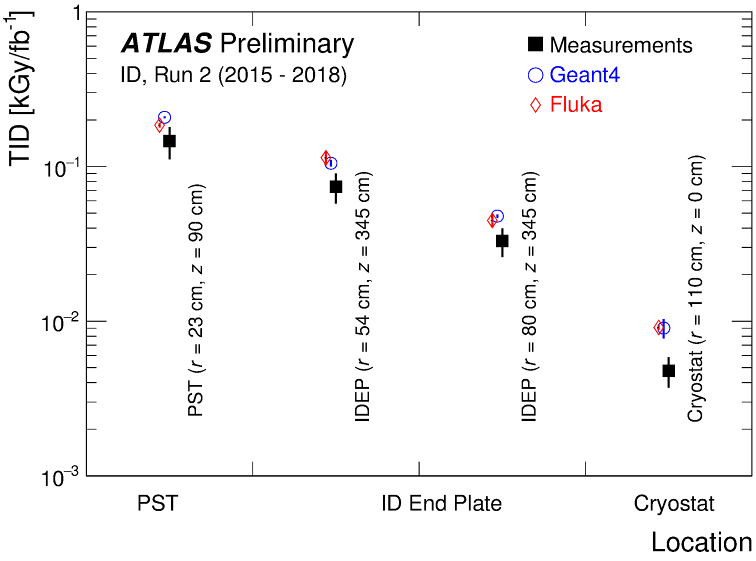

Fig. 26: Comparison of measurements with RadMon monitors and simulated TID at several locations inside the ID volume. One set of monitors is close to the IP, fixed on the pixel support tube (PST). Two sets are at different radii on the ID end plate, next to the endcap calorimeter, and a fourth set on the wall of the cryostat of the solenoid.

4.4.2 CMS

4.4.2.1 CMS simulation set-up

CMS typically uses FLUKA for radiation background simulations although MARS is used on occasion when quick turnaround simulations are required. The FLUKA simulation infrastructure is maintained by the Beam Radiation Instrumentation and Luminosity (BRIL) Project. FLUKA simulations are performed using the CERN Batch Service.

4.4.2.2 CMS FLUKA geometry description

In order to predict the radiation levels inside the CMS detectors, the complete detector and experimental cavern must be represented. The CMS FLUKA model includes the detector systems, shielding elements, services and beam-line components, the cavern floor and walls, and basic representations of cavern elements (main supports structures and electronics racks). The level of detail for the CMS FLUKA model inner detectors in terms of material composition and spatial resolution of regions is similar to that of the ATLAS FLUKA model.

Figure 27 shows the inner detector region as described in the FLUKA geometry. The central detectors are constructed with cylindrical shapes, and simulation results are therefore typically symmetric around the azimuthal angle ϕ, reducing necessary simulation time to obtain results with a small statistical uncertainty. For most predictions related to radiation damage, accurate results are produced so long as the total material radiation and interaction lengths are correctly implemented. However, an increasingly detailed representation of various structures is required so that localized effects are simulated in regions near the damage threshold. This often includes the implementation of ϕ asymmetric structures, for example, near the tracker bulkhead and LHC vacuum equipment. Advances in computing and use of batch computing means that corresponding results produced in a finer spatial binning structure are still possible within a reasonable time frame.

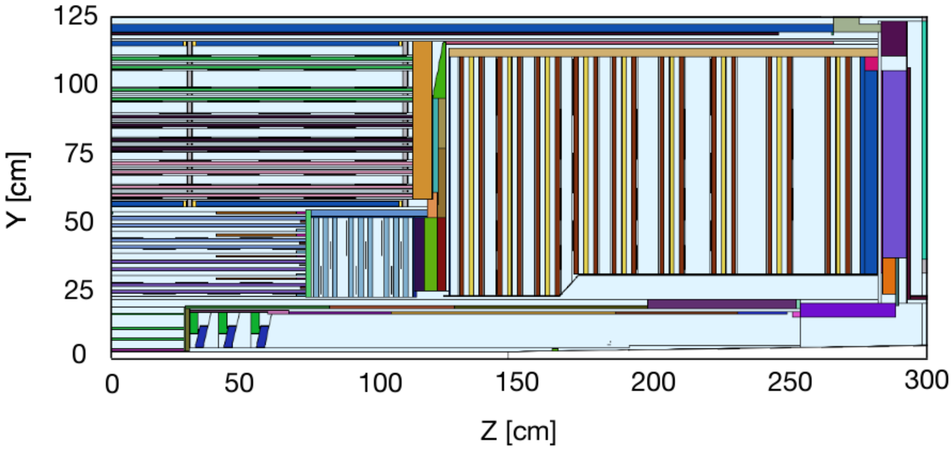

Fig. 27: A $Z - Y$ cut of the tracker region in the CMS FLUKA model

The CMS FLUKA geometry is frequently updated to include actual changes to the detector configurations, such as new shielding and beam pipe elements as well as to make general improvements to the representation of existing components. Future detector geometries are updated as upgrade designs evolve and several geometry models for past detector configurations are maintained for benchmarking purposes.

4.4.2.3 CMS FLUKA fluence and dose predictions

Figure 28 shows all particle contributions to the $\Phi_{\mathrm{eq}}^{\mathrm{Si}}$ and absorbed dose in the CMS inner detector resulting from proton–proton collisions. Here, $R4$ is the radial distance from the beamline and Z the distance from the IP following the direction of the beamline, and the results are averaged over the full ϕ range. In standard operation, collisions are the main source of radiation in the CMS central detectors and contributions from the LHC beam halo, or 'beam induced background', can be considered negligible. At the time of writing, estimates of the $\Phi_{\mathrm{eq}}^{\mathrm{Si}}$ use the in-built weighting factors for NIEL damage included in the FLUKA code.

The radiation field in the tracker volume is influenced by the 3.8 T magnetic field, the scattering on tracker material and vacuum chamber elements, as well as the backscattering from the surrounding

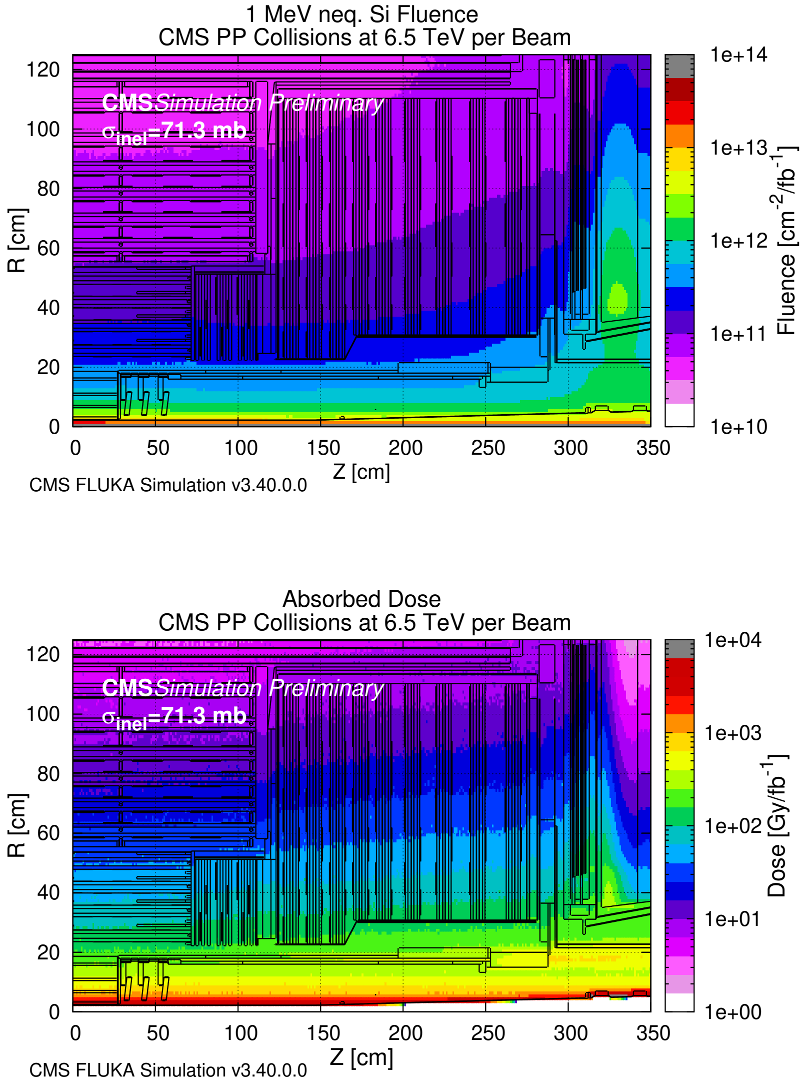

Fig. 28: The 1 MeV neutron equivalent fluence (top) and absorbed dose (bottom) in the CMS inner detector. The minimum-bias pp events are simulated with DPMJET-III at 13 TeV centre-of-mass energy and results are normalized to 71.3 mb inelastic cross-section. Simulations were performed with the FLUKA 2011 code using a Run 2 geometry model of CMS representing the 2018 configuration.

heavier detector elements, in particular the electromagnetic calorimeter crystals of the ‘ECAL endcap’ situated at approximately 3.2 m in Z. Figure 29 shows the relative contributions of various particle types to the $\Phi_{\mathrm{eq}}^{\mathrm{Si}}$ as a function of radius at two Z locations. The detectors exposed to the highest levels of total $\Phi_{\mathrm{eq}}^{\mathrm{Si}}$ are the pixel barrel which is situated around the IP and extends from a radius of 3.0 cm to 16.0 cm and the forward pixel regions which are situated between 29 cm and 60 cm in Z from the IP and extend into the $|\eta| > 2.5$ range. Here, $\Phi_{\mathrm{eq}}^{\mathrm{Si}}$ is dominated by the pion component. In the remaining tracker region, the high eta range in the tracker endcap (TEC) and layers close to the ECAL endcap at low radius are exposed to the highest $\Phi_{\mathrm{eq}}^{\mathrm{Si}}$ rates.

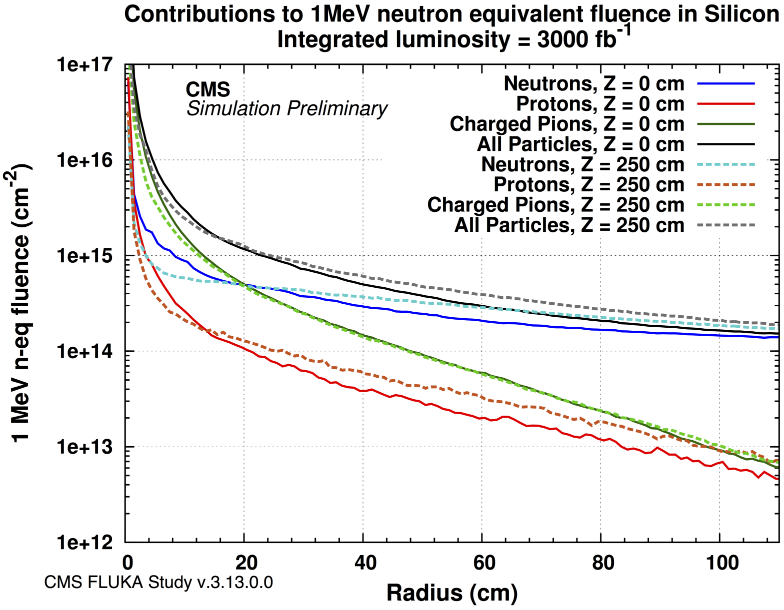

Fig. 29: Value of “$\Phi_{\mathrm{eq}}^{\mathrm{Si}}$ in the CMS tracker region estimated using the 2011 FLUKA code and a Run 2 geometry model. The minimum-bias pp events are simulated with DPMJET-III at 14 TeV centre-of-mass energy and results are normalized to 71.3 mb inelastic cross-section. The “All Particles” curve shows the total amount of $\Phi_{\mathrm{eq}}^{\mathrm{Si}}$. The Neutrons, Protons, and Charged Pions curves show the contribution to the $\Phi_{\mathrm{eq}}^{\mathrm{Si}}$ only from the respective particles.

4.4.2.4 Comparison of simulated predictions with measurements

Data that can be used for comparison with simulation include measurements of detector degradation; direct data from the subdetectors, which require special triggers and more complex analysis; measurements with passive and active radiation monitoring systems installed by the CMS BRIL project or other CERN groups; and measurements of the residual radiation field from activated components.

Section 5 describes measurements of the leakage current and depletion voltage in the CMS pixel and strip detectors and their comparisons with predictions based on FLUKA simulations and damage models. The leakage current, measured for each layer in the strip detector, and predictions agree with the data within 20%. For depletion voltage data and corresponding predictions, agreement is generally within 10%.

Whilst not the optimal for benchmark of $\Phi_{\mathrm{eq}}^{\mathrm{Si}}$, successful comparisons of FLUKA predictions with measurements of the residual radiation field from activated material in the tracker and central beampipe regions [28, 29] provide confidence in the relevant parts of the simulation set up for fluence and dose predictions, i.e., the production and transport of prompt radiation and the representation of materials in the CMS geometry model.

RAMSES ionization chamber monitors [30] installed by the HSE/RP group have been used successfully to benchmark energy deposition at various locations in the CMS experimental cavern with predictions and measurements being well within a factor 2 [28], a reasonable agreement for the outer cavern locations. Comparisons of FLUKA predictions with measurements from LHC RadMons installed by the EN/STI group for the high energy hadron (HEH) fluence, TID, and $\Phi_{\mathrm{eq}}^{\mathrm{Si}}$ at the cavern walls seem promising. However, remote switching ability between two modes for measuring either HEH or thermal neutron fluence is necessary for provision of independent data which currently require some FLUKA input. This will be available for Run 3.

4.4.3 LHCb

The LHCb experiment uses FLUKA for simulating radiation background in the spectrometer and detector cavern. The geometry description is simplified compared to the real detector, but contains the most relevant parts of all subdetectors, the LHC tunnel (with magnets) and support structures. The geometry has been continually updated and improved since its first implementation in the early phase of the experiment.

A set of radiation detectors were installed in the LHCb experimental area to measure different aspects of its radiation environment, allowing comparisons with the FLUKA predictions for TID and 1 MeV neutron fluence equivalent ($\Phi_{\mathrm{eq}}^{\mathrm{Si}}$). The neutron equivalence fluence simulated in the inner part of the detector is shown in Fig. 30. The main source of particle radiation is prompt production of particles in proton–proton collisions. This component is dominant in silicon VELO sensors which are situated at 8 mm from the interaction point. Further away from the interaction point particles produced in secondary interactions in the detector material become more dominant.

The radiation field in the LHCb spectrometer has a strong radial dependence. This is especially visible in the VELO sensors, where the fluence increases by an order of magnitude across the sensor radius, see Fig. 31 (left). During Run 1 and Run 2 the LHCb spectrometer collected an amount of data corresponding to 3.22 fb^{-1} and 6 fb^{-1} of integrated luminosity, respectively. The evolution of $\Phi_{\mathrm{eq}}^{\mathrm{Si}}$ is depicted in Fig. 31 (right). This distribution shows the differences between sensors situated at different z positions along the beam line. Considering the strong $\Phi_{\mathrm{eq}}^{\mathrm{Si}}$ dependence on radius r, it was noted that the fluence in the inner part of the sensors reached almost 6.7 $\times 10^{14}$ cm^{-2}.

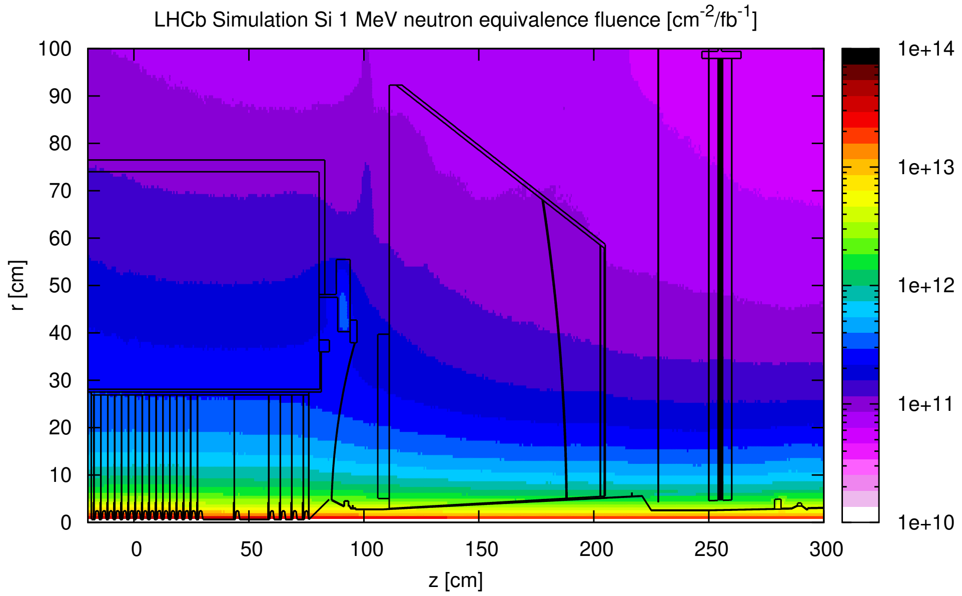

Fig. 30: Value of $\Phi_{\mathrm{eq}}^{\mathrm{Si}}$ in the LHCb trackers. The VELO sensors are perpendicular to the beam line and are visible in the bottom left corner.

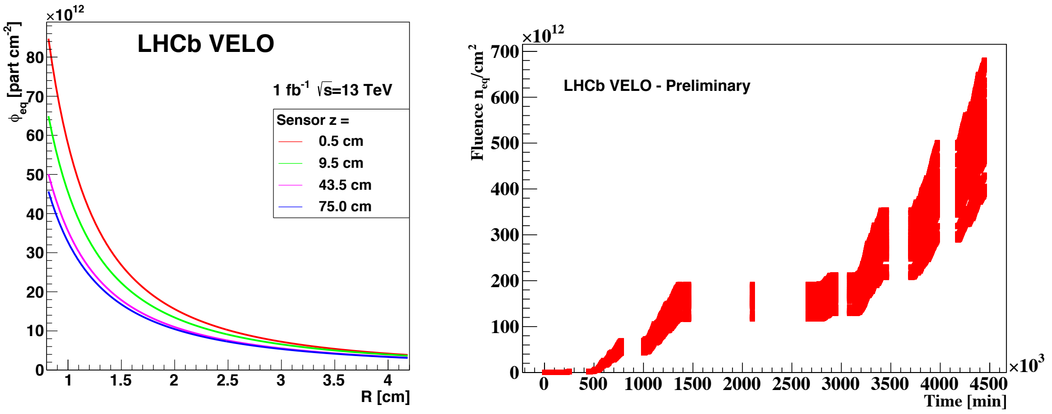

Fig. 31: Left: Radial dependency of the FLUKA simulation of $\Phi_{\mathrm{eq}}^{\mathrm{Si}}$ at a few representative LHCb VELO sensor positions. Right: Simulation of the evolution of $\Phi_{\mathrm{eq}}^{\mathrm{Si}}$ in the inner part ($0.8 < R < 1.1$ mm) in the LHCb VELO sensors during Run 1 and Run 2. Points represent the sensors situated at different z positions. The integrated luminosity delivered to the LHCb spectrometer reached 10 fb^{-1} of data.

4.4.4 ALICE

Given the requirement to run at reduced luminosity, the fluence seen by the innermost layer of the ALICE pixel detector, placed at a radius of $R = 3.9$ cm from the beam axis, was significantly lower with respect to the other LHC pixel detectors ($\Phi_{\mathrm{eq}}^{\mathrm{Si}} \sim 3.2 \times 10^{11}/\mathrm{cm}^2$ integrated throughout Run 1 and Run 2). Although these levels are not very severe, compared, for instance, with the levels in ATLAS and CMS, all components used in the ALICE inner tracking system (ITS) design were tested for their radiation hardness to levels exceeding significantly the expected doses, and full radiation tolerant technologies have been used throughout the system for critical components, such as the front-end electronics. In particular, the chips of the two innermost layers of the ITS detector were qualified for a radiation in exceed of 10 Mrad [31]; this explains the extremely low failure rate observed, even though radiation effects were not completely absent, as reported in Ref. [32].

Single event upset (SEU) events have also been observed in the silicon strip detector, in particular affecting the SRAM FPGA of the front-end read out modules (FEROM) [32]. Figure 32 shows the integrated number of SEUs since 2015, together with the integrated fluence of high-energy hadrons (HEH), measured by a RadMon sensor installed near the FEROM crate. No SEUs were expected, since the FEROM modules are located in the experiment cavern in a region where the TID at the end of Run 2 was 0.34 krad. Anyway, the linear correlation between SEU occurrences and fluence indicates that the SEU cross-section did not increase during Run 2. As mitigation measures, after LS1 a radiation tolerant PROM was used and a firmware upgrade allowing faster FPGA reload was implemented.

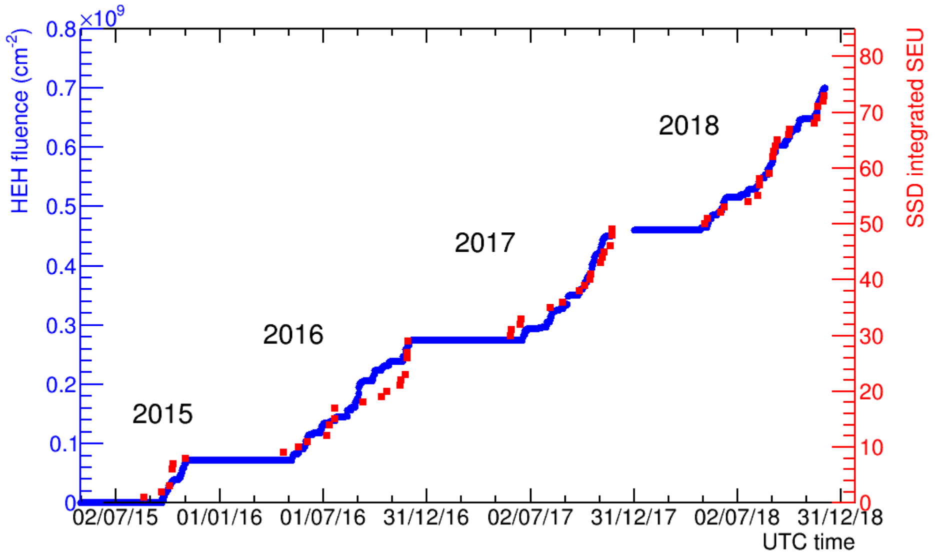

Fig. 32: Observed SEU occurrences in the SSD front-end readout modules and high-energy hadron fluence at the modules position, as a function of time

Simulations of the radiation environments were focused initially only on beam losses, in particular during injection, since ALICE is close to the Beam 1 transfer line from the SPS into the LHC. During Run 1, however, as explained in Section 4.4.4.1 below, a degradation of the vacuum conditions in the Long Straight Section 2 led to a new detailed study of the beam-induced background [33]. More recently, in view of the comprehensive upgrade planned for Run 3, when the experiment will face increasing collision rates, new studies have been performed [34], in particular to assess the radiation load of the new ITS, the first large scale application of the monolithic active pixel sensor in a HEP experiment. The radiation simulations for the ALICE experiment are performed within the AliRoot [35] framework, which provides a detailed geometry and material description of all detector layers, support structures, and beamline elements inside the experimental area. Electric and magnetic field maps are processed as well. Particle transport is performed with FLUKA [4, 5]. The transport cuts for the particle species are adjusted region by region according to their importance in order to optimize the computing time. The lowest cuts are used in the central barrel detectors, while in the outer regions these cuts are raised considerably in order to save CPU time. The lowest kinetic energy cutoff for photon, electron, neutral, and charged hadron and muon transport is set to 1 keV and down to thermal energies of 293 K for neutron. The threshold for electron and muon delta-ray production is 30 keV, as well as for electron and muon bremsstrahlung and for electron pair production by muons.

The simulations are based on 50 000 minimum-bias proton–proton events at a centre-of-mass energy of 5.5 TeV, simulated using the PYTHIA6 event generator (Perugia-2011 tune). The 1 MeV neutron equivalent fluence ($\Phi_{\text{eq}}^{\text{Si}}$) and the TID are the numbers that determine the long-term radiation damage of sensors and electronics. The rate of hadrons with a kinetic energy > 20 MeV determines the rate of stochastic failures, like single event upsets in the microelectronics circuitry. The fluence of all the charged particles is not directly linked to radiation-induced effects; nevertheless, it determines the detector occupancy and influences track reconstruction and particle identification and was therefore calculated along with the above mentioned quantities. The FLUKA USRBIN function, that allows the distribution of one or several quantities of interest to be scored in a regular spatial structure independent from the geometry, is used in the calculations. All results were obtained by superimposing a $r - z$ cylindrical mesh, with the cylinder axis parallel to the z-axis, on top of the ALICE geometry; the scored quantities are averaged along the azimuthal angle φ. Results from the USRBIN function are normalized per unit volume and per unit primary weight. Different meshes were defined to score the relevant quantities with the appropriate granularity. The bin size ranges from 1 mm $\times$ 5 mm for the innermost layers of the silicon detectors to 1 cm $\times$ 2.5 cm for the outermost ALICE detectors.

The dose and the neutron equivalence fluence simulated in the inner part of the detector are shown in Fig. 33 for the whole Run 1 and Run 2 physics program. At positions with $-100 < \text{z} < 250$ cm, the radiation numbers are dominated by primary tracks originating from the interaction point. At $z < -100$ cm the front absorber of the muon spectrometer is stopping hadrons that are pointing towards the muon system, which leads to a decrease of the TID but an increase of the hadron fluence due to the lateral escape of neutrons. The innermost ALICE detectors are exposed to a TID close to a few tens of krad and a fluence up to 10^{11} cm^{-2}.

4.4.4.1 Contribution of beam-gas background

The moderate interaction rates in Run 1 and Run 2 meant that ALICE had the most unfavourable ratio of collision rate over background rate. In addition, after the beam intensity ramp up in 2011, a degradation of vacuum upstream of the UX25 was observed, producing a large beam-gas background reaching $\sim 20\%$ of the collision rates.

The machine-induced background is mainly ascribed to inelastic interactions of beam protons with residual gas molecules in the so-called long straight section (LSS2). The observed nearly linear correlation between background rates measured in ALICE and the product of the bunch intensity times the average vacuum pressure in the LSS2 provides a further confirmation of this assumption. The pressure in the LSS2 easily exceeded the 10^{-8} mbar both in the 2011 and 2012 pp fills with more than 1000 circulating bunches. In the UX25 cavern, on the contrary, it has been measured to be constantly around 1–0.5 $\times 10^{-10}$ mbar, below 10^{13} molecules/m^3 hydrogen-equivalent gas density. The contribution of beam-gas interactions inside the cavern can therefore be neglected for the computation of the beam background simulations. Due to the proportionality of the dynamic gas pressure and the TDI outgassing to the beam intensity, their relevance for Pb–Pb as well for p–Pb runs is orders of magnitude lower than for pp, as confirmed by ALICE measurements. Beam-gas interactions were simulated by distributing proton–H_2 inelastic interactions along the LSS2 according to a detailed pressure profile provided by the CERN TE-VSC group in 2012 and based on the pp reference fill 2736. So far, only the machine-induced background from the IR2 left side of ALICE has been simulated; however, due to the presence of the beam 1 injection

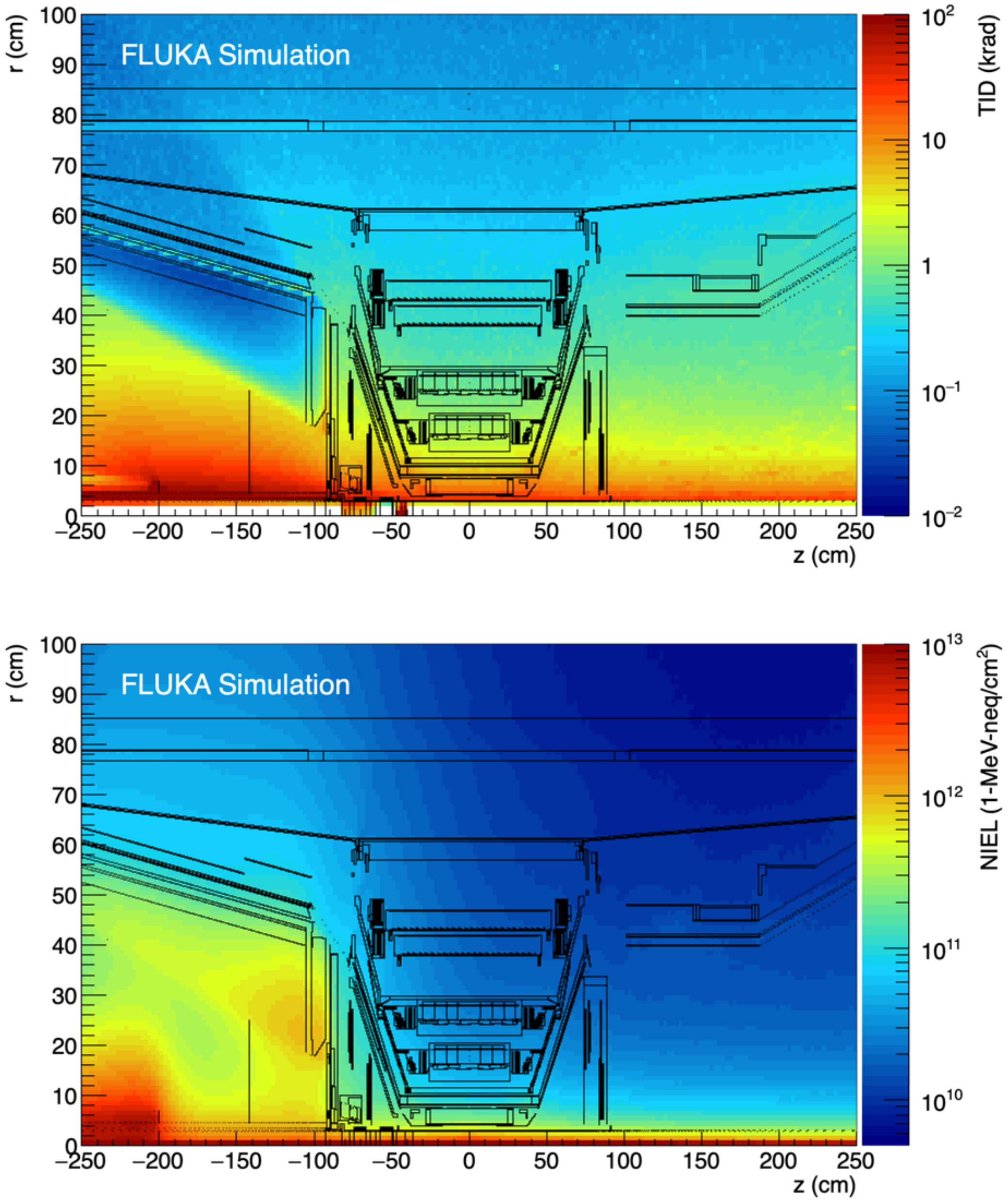

Fig. 33: TID (top) and Φ_{eq}^{Si} (bottom) in ALICE. The values correspond to the Run 1 and Run 2 physics programs.

line and the TDI, this background is by far the most dominant one in ALICE.

The p–H_2 interactions were computed with DPMJET [9] and the total rate of inelastic interactions in the LSS2 was calculated from the integral of the pressure profile. The cascade of the p–H_2 collisions were calculated using a detailed FLUKA modelling of the LSS2 (from UJ23 until ALICE cavern) performed by the LHC FLUKA Group in 2012 with a very accurate vacuum layout. A transport cutoff of 20 MeV has been applied in order to save CPU time. All the particles reaching the scoring plane 20 m away from the IP2 are then transported using FLUKA. In the present simulation 50 000 primary beam-gas interactions have been considered.

4.4.4.2 Comparison of simulated predictions with measurements

A comparison between simulated and measured dose in ALICE was performed by means of radiation monitors (RadMon) in order to validate the radiation calculations. The RadMon system has been developed by the CERN Engineering (EN) department; it includes RadFETs for TID measurements, silicon p–i–n diodes for the 1 MeV equivalent neutron fluence, and SRAM memories for the high-energy hadron and thermal neutron fluence. In Fig. 34, the trend versus time of the TID measured during the 2017 pp fills by the RadMon sensor called D12, located 480 cm away from the IP2 and 34 cm from the beam axis, is reported and compared with prediction from simulation. The expected TID is obtained by multiplying the ALICE delivered luminosity by the inelastic pp cross-section at $\sqrt{s}$ = 13 TeV and the simulated TID per pp collision at the sensor location scaled for the average charged-particle multiplicity density ratio $(\mathrm{d}N_{\mathrm{ch}}/\mathrm{d}\eta(13\mathrm{TeV}))$ / $(\mathrm{dN}_{\mathrm{ch}}/\mathrm{d}\eta(5.5\mathrm{TeV}))$. The measured TID is well reproduced by the expected dose due to genuine pp collisions at IP2, thus implying a negligible contribution from machine-induced background to the total dose, which is expected considering the low beam-gas rates measured in ALICE throughout the 2017 and the RadMon sensor location.

A further comparison was performed with 2018 pp data after having moved the D12 sensor closer to the beam axis and downstream of the massive vacuum equipment at $z \sim 4$ m from IP2 (new location at 340 cm away from the IP2 and at 20 cm from the beam axis). The comparison is reported in Fig. 35. To evaluate the radiation load due to the machine-induced background, an estimation of the total number of primary beam-gas interactions in the LSS2 (left side) throughout the 2018 pp fills is needed. This is estimated as the integral of the trend versus time of the average vacuum pressure in the LSS2, evaluated as the arithmetic average of pressure in the TDI and in the inner triplet ITL2, multiplied by the beam 1 intensity, the LHC revolution frequency, and the probability that a proton traversing the LSS2 has an inelastic nuclear interaction with a residual gas nucleus. The latter was obtained based on p–H_2 interactions computed with DPMJET and on the Run 1 pressure profile normalized to the Run 2 average vacuum pressure. The expected dose was then derived by multiplying the expected total beam-gas interactions in 2018 by the simulated dose per beam-gas interaction at the sensor location. The measurements can be reproduced by simulation including pure pp collisions at the IP and beam gas from LSS2. The dose of 2.0×10^{-13} krad per pp collision shown in Fig. 35 is the value that better reproduces the TID measured by the D12 sensor during the 2018 Pb–Pb fills, where the contribution of beam gas to the total dose is expected to be negligible because of the low intensity of the Pb beams, while 2.0×10^{-13} krad per beam-gas interaction is the outcome of our simulation. The overall contribution from beam gas in 2018 is, however, expected to be very low, thus making it difficult to draw firm conclusions on the reliability of our beam-gas simulation since the measurements can be also reproduced assuming a negligible contribution from machine-induced background even during the pp fills. However, such comparison suggests that the aforementioned calculations can be interpreted as an upper limit for machine-induced background contribution to the total dose.

4.4.4.3 Detector specifications for Run 3 and Run 4

After the second LHC Long Shutdown, the luminosity with lead beams will gradually increase to an interaction rate of 50 kHz, leading to a data rate that the current ALICE electronics and detectors cannot process. The upgrade of the experiment is mainly focused on increasing the readout rate capability to record the full 50 kHz of Pb–Pb interactions. A fundamental element of the upgrade strategy is the new, high-resolution, ultra-light ITS based on MAPS (monolithic active pixel sensor) [36]. The ALPIDE chip is a 15 mm × 30 mm large MAPS, implemented in a 180 nm CMOS imaging sensor process by TowerJazz [2]. Material budget constraints require the usage of sensors thinned to 50 μm in the IB, while 100 μm thick sensors are employed in the outermost layers. The novel implementation of deep p-well in the process allows full CMOS circuitry within the pixel matrix, still keeping full charge collection efficiency [37–39]. A very low power consumption of less than 40 mW/cm^2 has been achieved thanks to

---

[2] Tower Jazz, http://www.jazzsemi.com

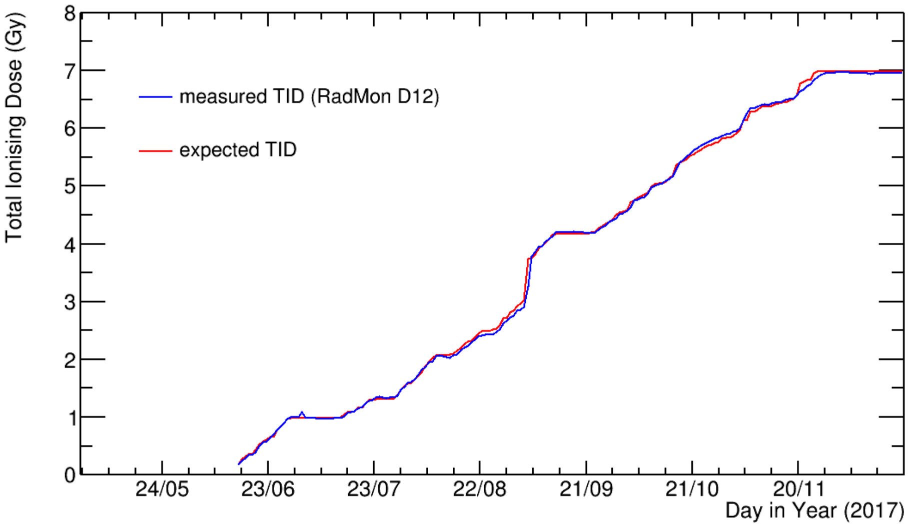

Fig. 34: Trend of the accumulated TID during 2017 from measurements by RadMon sensor (blue line) and simulations (red line).

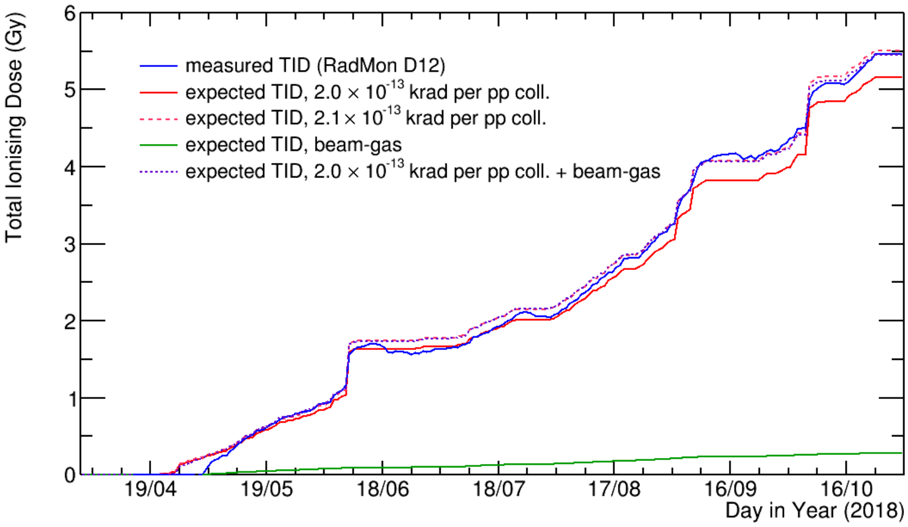

Fig. 35: Trend of the accumulated TID during 2018 from measurements by RadMon sensor (blue line) and simulations.

the integration of continuously active low-power front end into each pixel and in-matrix zero suppression circuit (‘Priority encoder’). The sensor is segmented into 512 × 1024 pixels of 29 μm × 27 μm; a periphery circuit region of 1.2 mm × 30 mm implements control, and readout functionalities.

From the doses and fluences simulated for IP collisions and the background assumptions, the specifications for the ALICE detector systems in Run 3 and Run 4, including safety factors, can be derived, taking into account the recent results on measured multiplicities for Pb–Pb, pp, and p–Pb collisions. Results for different colliding systems and energies are derived by scaling the simulated values by the average charged-particle multiplicity density reported in Table 7, where an extended running scenario for

Table 7: Extended running scenario for the ALICE operation after LS2; $\int \mathcal{L}$ and L_{peak} stand for integrated and peak luminosity respectively, σ_{t} for inelastic cross-section, and η for pseudorapidity.

	pp 14 TeV	**p–Pb** 5.5 TeV/NN	**Pb–Pb** 5.5 TeV/NN
$\int \mathcal{L}(\text{nb}^{-1})$	2.5 10^5	1000	13
$L_{\text{peak}}(\text{cm}^{-2}\text{s}^{-1})$	6.0 10^{30}	1.0 10^{29}	6.25 10^{27}
σ_{t} (mb)	80	2000	8000
Peak rate (s^{-1})	4.2 10^5	2.0 10^5	5 10^4
Events	2 10^{13}	2.0 10^{12}	10.4 10^{10}
$\text{d}N_{\text{ch}}/\text{d}\eta$	6.46	18.4	492.5
peak rate of tracks N_{ch}/η (s^{-1})	2.7 10^6	3.7 10^6	25 10^6
total Nr. of tracks N_{tot}/η	129.2 10^{12}	36.8 10^{12}	51.2 10^{12}

Run 3 and Run 4 even more ambitious than the plan reported in the ALICE Upgrade LOI [40] is shown, under the assumption that the shape of the $\text{d}N_{\text{ch}}/\text{d}\eta$ distribution does not differ significantly for the different colliding systems. The charged-particle multiplicity densities at midrapidity have been obtained by scaling the ALICE measured multiplicities [41–44]. A scaling factor of $s_{NN}^{0.15}$ ($s_{NN}^{0.11}$) has been applied to Pb–Pb (p–Pb and pp) to obtain the values for the centre-of-mass energy of $\sqrt{s_{NN}}$ = 5.5 TeV. The last row in Table 7 represents the expected total number of charged particles per unit of pseudorapidity integrated for Run 3 and Run 4. Since the radiation load is directly correlated with the total number of produced particles, in this scenario the pp collisions would represent 59% of the total ionizing dose and high-energy hadron fluence, while p–Pb and Pb–Pb collisions account for 17% and 24%, respectively.

The sum of the two contributions (IP collisions and beam gas) gives the best estimate for the radiation load of ALICE, on top of which a safety factor ten was multiplied. Concerning the beam-gas collisions, an improvement of the vacuum conditions by a factor of 10 with respect to Run 1 is assumed, i.e., an average vacuum pressure of $< 2.3 \times 10^{-9}$ mbar in the LSS2 around ALICE. The resulting numbers are shown in Table 8. With the extended running scenario, the TID contributions from collisions and beam-gas background are quite similar, while the NIEL is dominated by collisions. This is not surprising considering that the background consists almost entirely of electromagnetic radiation (mostly photons, then electrons).

Table 8: Specified radiation numbers for the 7 layers of the new ALICE ITS for a physics program of 13 nb^{-1} Pb–Pb + 1 pb^{-1} p–Pb + 6 pb^{-1} pp at 5.5 TeV + 250 pb^{-1} pp at 14 TeV collisions, assuming an operational efficiency of 77%, a vacuum pressure of 2.3×10^{-9} mbar in the Long Straight Sections around ALICE, and a safety factor of 10.

Element	**TID (krad)**	**1-MeV-neq (cm^{-2})**
ITS L0	5602	5.78×10^{13}
ITS L1	3810	3.97×10^{13}
ITS L2	2310	2.58×10^{13}
ITS L3	130	2.46×10^{12}
ITS L4	106	2.17×10^{12}
ITS L5	36	1.44×10^{12}
ITS L6	33	1.40×10^{12}

4.5 Discussion and outlook

In this chapter we have shown how Monte Carlo particle event generators and particle transport codes have been used to successfully simulate radiation backgrounds in and around the LHC experiments. We showed how the proton–proton collisions are now well described by Monte Carlo events generators such as PYTHIA, with inelastic cross-sections and particle productions rates described at levels of precision typically less than 10%. The validation of the simulations by comparison with measurements has led to an improved understanding of the uncertainties involved. For example, in the initial design phase of ATLAS, factors of 2–5 were applied by some of the experiments to reflect the uncertainties in the simulations. Today, a factor 1.5 on simulated predictions of fluence and dose is used in HL-LHC upgrade studies. This in turn has enormous implications on the choice of technologies that can be used in the LHC experiment upgrades, which in turn has enormous cost benefits. An important caveat to this, however, is that the reliability and accuracy of the simulation results are highly dependent on the geometry and material description of the experiment implemented in the simulations. For radiation background studies the fine detail is often not required, but it is crucial to reproduce accurately the radiation and interaction lengths. A final comment on 'lessons learned' is relevant for detector upgrades in an experiment. It is vital to study the impact of introducing new detector systems and services into an existing experiment, otherwise unintended increases in radiation background levels can occur in some of the other systems leading to a reduction in detector lifetime.

References

[1] ATLAS Collaboration, *JINST* **13** (2018) P12006, doi:10.1088/1748-0221/13/12/P12006.

[2] T. Sjöstrand, S. Mrenna, P. Skands, *JHEP* **05** (2006) 026, 10.1088/1126-6708/2006/05/026; *Comput. Phys. Comm.* **178** (2008) 852–867, doi:10.1016/j.cpc.2008.01.036.

[3] S. Roesler, R. Engel, J. Ranft, The Monte Carlo Event Generator DPMJET-III, International Conference on Advanced Monte Carlo for Radiation Physics, Particle Transport Simulation and Applications (Springer, Berlin, 2001), pp. 1033–1038, doi:10.1007/978-3-642-18211-2_166, arXiv:hep-ph/0012252.

[4] G. Battistoni *et. al.*, *Ann. Nucl. Energy* **82** (2015) 10, doi:10.1016/j.anucene.2014.11.007.

[5] T.T. Bohlen *et. al.*, *Nucl. Data Sheets* **120** (2014) 211, doi:10.1016/j.nds.2014.07.049.

[6] I.L. Azhgirey and V.V. Talanov, MARS software package status, Proc. 17. Conference on Charged Particle Accelerators ([s.n.], Protvino, 2000), vol. 2, p. 184.

[7] S. Agostinelli *et al.* [GEANT4 Collaboration], *Nucl. Instrum. Methods Phys. Res.* **A506** (2003) 250, doi:10.1016/S0168-9002(03)01368-8; J. Allison *et al.*, *IEEE Trans. Nucl. Sci.* **53** (2006) 270, doi:10.1109/TNS.2006.869826; J. Allison *et al.*, *Nucl. Instrum. Methods Phys. Res.* **A835** (2016) 186, doi:10.1016/j.nima.2016.06.125.

[8] R. Engel, *Z.Phys.* **C66** 203 1995, doi:10.1007/BF01496594; R. Engel, J. Ranft, *Phys.Rev.* **D54** (1996) 4244, doi:10.1103/PhysRevD.54.4244, arXiv:hep-ph/9509373.

[9] J. Ranft, *Phys. Rev.* **D51** (1995) 64, doi:10.1103/PhysRevD.51.64.

[10] ATLAS Collaboration, *Eur. Phys. J.* **C76** (2016) 502, doi:10.1140/epjc/s10052-016-4335-y.

[11] LHCb Collaboration, *Eur. Phys. J.* **C74** 2014 2888, doi:10.1140/epjc/s10052-014-2888-1.

[12] CMS Collaboration, *Eur. Phys. J.* **C78** (2018) 697, doi:10.1140/epjc/s10052-018-6144-y.

[13] ATLAS Collaboration, *Phys. Rev. Lett.* **117** (2016) 182002, doi:10.1103/PhysRevLett.117.182002.

[14] FLUKA web site, (CERN, Geneva), last accessed July 15 2020.

[15] A. Capella *et al.*, *Phys. Rep* **236** (1994) 225, doi:10.1016/0370-1573(94)90064-7.

[16] A. Ferrari and P.R. Sala, The physics of high energy reactions, Proc. Workshop on Nuclear Reaction Data and Nuclear Reactors Physics, Design and Safety, Eds. A. Gandini, G. Reffo (World Scientific, Singapore, 1998), pp. 424–532, doi:10.1142/9789814530385, ATL-PHYS-97-113.

[17] A. Ferrari, P.R. Sala, A new model for hadronic interactions at intermediate energies for the FLUKA code, Proc. MC93 Int. Conf. on Monte Carlo Simulation in High Energy and Nuclear Physics Eds. P. Dragovitsch *et. al.* (World Scientific, Singapore 1994), pp. 277-288, doi:10.1142/9789814534833.

[18] A. Fassò *et. al.*, FLUKA: performances and applications in the intermediate energy range, Proc. OECD / NEA Specialists' Meeting on Shielding Aspects of Accelerator, Targets and Irradiation Facilities, (OECD, Paris 1995), pp. 287-304.

[19] A. Ferrari *et al.*, *Z. Phys.* **C71** (1996) 75, doi:10.1007/s002880050149, arXiv:nucl-th/9603010.

[20] A. Ferrari *et al.*, *Z. Phys.* **C70** (1996) 413, doi:10.1007/s002880050119, arXiv:nucl-th/9509039.

[21] C. Zeitnitz and T.A. Gabriel, *Nucl. Instrum. Meth.* **A349** (1994) 106, doi:10.1016/0168-9002(94)90613-0.

[22] M. Huhtinen and F. Faccio, *Nucl. Instrum. Meth.* **A450** (2000) 155, doi:10.1016/S0168-9002(00)00155-8.

[23] ATLAS Collaboration, Summary of ATLAS Pythia 8 Tunes, ATL-PHYS-PUB-2012-003 (CERN, Geneva, 2012).

[24] J. Boudreau et al, The GeoModel Toolkit for detector description, Proc. Computing in High Energy Physics and Nuclear Physics 2004, Eds. A. Aimar, J. Harvey, N. Knoors (CERN, Geneva, 2005), p. 353 doi:10.5170/CERN-2005-002.353.

[25] ATLAS Collaboration *JINST* **3** (2008) S08003, doi:10.1088/1748-0221/3/08/S08003.

[26] I. Mandić *et al.*, *IEEE Trans.Nucl.Sci.* **54** (2007) 1143, doi:10.1109/TNS.2007.895120.

[27] I. Mandić *et al.*, First results from the online radiation dose monitoring system in ATLAS experiment, 2011 IEEE Nuclear Science Symposium Conference Record, Valencia, 2011, pp. 1107-1112, doi: 10.1109/NSSMIC.2011.6154582.

[28] J. Wańczyk, Measurements and estimates of the radiation levels in the CMS experimental cavern using Medipix and RAMSES monitors, and the FLUKA Monte Carlo code, Master thesis, AGH Univ. Sci. Tech., Kraków, 2019.

[29] D. Bozzato, Simulations for the CMS radiation field: results for shutdown scenarios and benchmarks, Laurea, Polytech. Univ. Milan, 2019.

[30] G. Segura *et al.*, RAMSES: the LHC radiation monitoring system for the environment and safety, Proc. 10th Int. Conf. on Accelerator and Large Experimental Physics Control Systems (JACoW, Geneva, 2005), TH3B.1-3O.

[31] ALICE Collaboration, *JINST* **3** (2008) S08002, doi:10.1088/1748-0221/3/08/S08002.

[32] E. Botta, *PoS* **Vertex2019** (2020) 002, doi:10.22323/1.373.0002.

[33] ALICE Collaboration, Performance of the ALICE Experiment at the CERN LHC, *Int. J. Mod. Phys.* textbfA29 (2014) 1430044, doi:10.1142/S0217751X14300440.

[34] A. Alici *et al.*, Radiation dose and fluence in ALICE after LS2, ALICE-PUBLIC-2018-012 (CERN, Geneva, 2018).

[35] ALICE Software Reference Manual, (CERN, Geneva), last accessed July 25 2020.

[36] ALICE Collaboration, *J. Phys.* **G41** (2014) 087002 doi:10.1088/0954-3899/41/8/087002.

[37] G. Aglieri Rinella, *Nucl. Instrum. Methods Phys. Res.* **A845** 2017 583 doi:10.1016/j.nima.2016.05.016.

[38] A. Di Mauro, *Nucl. Instrum. Methods Phys. Res.* **A936** 2019 625, doi:10.1016/j.nima.2018.10.047.

[39] M. Ŝuljić, *JINST* **11**(2016 C11025, doi:10.1088/1748-0221/11/11/C11025.

[40] ALICE Collaboration, *J. Phys.* **G41** (2014) 087001, doi:10.1088/0954-3899/41/8/087001.

[41] ALICE Collaboration, *Eur. Phys. J.* **C68** (2010) 345, doi:10.1140/epjc/s10052-010-1350-2.

[42] ALICE Collaboration, *Phys. Rev. Lett.* **110** (2013) 032301, doi:10.1103/PhysRevLett.110.032301.

[43] ALICE Collaboration, *Phys. Rev. Lett.* **105** (2010) 252301, doi:10.1103/PhysRevLett.105.252301.

[44] ALICE Collaboration, *Phys. Rev. Lett.* **116** (2016) 222302, doi:10.1103/PhysRevLett.116.222302.